A Comprehensive Analysis of a Digital Control Strategy for Photovoltaic-Based Single-Phase Grid-Tied Inverter Systems

Soheil Hasani Sangani
Department of ECE
Tarbiat Modares University
Tehran, Iran
0000-0003-4809-2074

Mohamad Reza Moslemnejad
Department of R&D
Behine-Sazan-Toos Company
Mashhad, Iran
moslemnezhad-m@bst.co.ir

Mojtaba Saeedi
Department of R&D
Behine-Sazan-Toos Company
Mashhad, Iran
saeedi-m@bst.co.ir

Alireza Jalalitalab
Department of Technical Management
Behine-Sazan-Toos Company
Mashhad, Iran
jalalitalab-a@bst.co.ir

Reza Beiranvand
Department of ECE
Tarbiat Modares University
Tehran, Iran
0000-0002-3214-7563

Abstract— **This paper generally presents the design procedure of a single phase grid-tied solar inverter and its control system. Moreover, it specifically investigates the behavior of the entire system to obtain its optimal compensators. The power section of the system contains a DC-DC stage followed by an inverter and its filters. Furthermore, the control system includes a maximum power point tracking (MPPT) algorithm, a phase locked loop (PLL), a current controller for shaping the injected current to the grid, and a voltage controller for regulating the voltage of the DC link between the boost converter and the inverter. This paper proposes a featured procedure to simulate the function of each compensator in the Laplace and z-domains, and implement it on a digital microcontroller device. Eventually, the simulation results of a PV-based system comprising a boost converter, a Highly Efficient and Reliable Inverter Concept (HERIC) inverter, and its compensators, operating at 20 kHz switching frequency, are presented.**

Keywords— Grid-tied inverter, renewable energy, phase locked loop (PLL), maximum power point tracking (MPPT), Highly Efficient and Reliable Inverter Concept (HERIC).

I. INTRODUCTION

Nowadays, due to the fossil fuels issues such as their shortage, contamination, carbon dioxide emission, global warming, etc., investigating an alternative for these kind of sources has become a necessity. Renewable energy sources including PV panels, wind turbines, and fuel cells, are considered the most desirable replacement for fossil fuels [1-5].

In addition to renewable energy, high step-up DC-DC converters are employed in other applications such as X-ray, laser, plasma, etc. These converters are considered an essential part of the PV-based systems, mainly because of the low output voltage that PV panels produce. High step-up DC-DC converters are preferred over connecting panels together, which can lead to mismatch and shading effects. To improve the performance of the conventional boost converter, which is not suitable for high voltage gains, several techniques and strategies are proposed in papers [6, 7]. Coupled-inductors (CIs) can be used to increase voltage gain and provide isolation in some cases. However, they may produce voltage spikes in addition to their weight-related issues [8]. Quadratic

boost (QB)-based networks and voltage multipliers (VMs) are also proposed as step-up techniques that can minimize voltage and current stresses. Although interleaving is not categorized as a step-up technique, it is widely used in DC-DC converters to reduce input current ripple [9- 11]. Soft switching, which is a common concept in DC-DC converters, can significantly reduce power loss, increase power density and switching frequency, and minimize the dimensions of the converter. Nevertheless, a tradeoff between the mentioned parameters and the number of the components is required in PV-based systems with many power switches involved [12- 14]. Mostly, a combination of the aforementioned techniques is used in high step-up DC-DC converters. [15] and [16] propose VM- and CI-based converters that achieve high voltage gains with low voltage and current stresses. [17] presents an efficient, high-gain, low-stress topology that combines all mentioned techniques without soft switching capability. These techniques can be considered as long as the number of elements does not critically decrease the efficiency or lead to unjustifiable costs. However, since this paper mostly concentrate on control schemes; a conventional boost converter is sufficient.

Traditional PV-based inverter systems often use transformers for isolation, which can lead to efficiency and cost issues. Therefore, transformerless structures seem to be a more suitable solution. Nonetheless, they are facing a leakage current problem, which flows through the ground, caused by the parasitic capacitor of the panel [18, 19]. To address the leakage current issue, DC decoupling-based inverters such as H5 and H6, and AC decoupling-based inverters such as HERIC topologies, have been proposed in the literature [20]. HERIC inverters provide higher efficiencies comparing to all other mentioned topologies. In addition, it has been observed that LCL filters offer better harmonic elimination characteristics than simple L filters in inverter circuits [21]. In [22], the authors propose a better switching pattern in terms of providing a bidirectional current path in freewheeling duration for reactive power injection in HERIC inverters, comparing to the conventional one in [23].

Regarding the V-I characteristic of a PV-panel, there is a point where it generates its maximum possible electric power for a specified irradiation value. To utilize the entire capacity of a PV panel, it must operate at its maximum power point

Fig. 1. PV-based grid-tied inverter system including power and control sections

(MPP) [24, 25]. There is a variety of methods to derive this maximum power from a PV panel, such as Fixed Duty Cycle, Constant Voltage, Perturb & Observe (P&O), Incremental Conductance (IC), and Ripple Correlation. A comparison of all mentioned methods is presented in [26]. For the purposes of this paper, the P&O method is considered, which is a common and simple algorithm to implement.

A phase-locked loop (PLL) is required to obtain the grid phase and frequency in grid-tied inverter systems. This paper considers a PLL block based on an orthogonal signal generator (OSG) [27, 28]. PV-based grid-tied inverter systems require a relatively complicated control system. In addition to the MPPT control on the DC-DC stage, an outer DC bus voltage control loop, and an inner AC current control loop are necessary on the DC-AC stage to regulate the DC bus voltage and determine the injected current to the grid, respectively [29]. Several methods are proposed in the literature for grid current control, such as deadbeat, hysteresis, predictive, proportional-integral (PI), and proportional-resonant (PR) [30]. PR controllers, which originally proposed in [31], are able to provide zero steady-state error in tracking a sinusoidal waveform comparing to PI compensators. Therefore, they are preferred in PV-based grid-connected inverter systems [32]. Nevertheless, to prevent stability issues can be caused by an unlimited gain, the non-ideal PR controllersو as mentioned in [33] are more preferable.

In this paper, a PV-based inverter system, including its power and control sections, is considered. The power section consists of a conventional boost converter to track the maximum power point (MPP) of the PV panel, followed by a HERIC inverter to process the panel's instantaneous maximum power, regulate the DC bus voltage, and shape the injected current to the utility grid. The switching pattern proposed in [22] is used to drive the inverter's power switches. The main purpose of this paper is to find the proper compensators, examine their z-domain transfer functions (TF) and difference equations by applying some different input signals to them and observe the output signals through computer simulation, and finally simulate the overall system. Eventually, a systematic procedure to obtain and implement the compensators for a PV-based grid-tied inverter system will be presented.

Section II provides a detailed description of the circuit topology, its controllers, and the switching pattern. Section III presents the simulation results of the converter prototype, and Section IV concludes the paper.

II. DESCRIPTION OF THE SYSTEM OPERATION

Fig. 1 demonstrates the circuit diagram of the overall system including power and control sections. The power section

comprises a boost converter driven by MPPT control block, and a HERIC inverter. The inverter and its control schemes are responsible for regulating the DC bus voltage and shaping the injected current to the grid. This section analyzes, discusses, and simulates the different stages of the system and their controllers in PSIM software.

A. DC-DC Satge and MPPT Control Block

As mentioned earlier, maximum power point tracking of a PV panel can be achieved using various methods. This paper prefers the P&O algorithm for its simple implementation and description. Although PSIM simulator provides examples to instruct users, this paper uses the P&O algorithm of Fig. 2. It has to be pointed out that the block diagram of Fig. 2 is applicable for PSIM simulator, exactly as it is indicated. The z-domain TFs of Fig. 2 can be expressed as follows:

Fig. 2. The block diagram of the P&O algorithm in PSIM simulator.

$$\begin{cases} H_\Sigma(z) = \dfrac{z}{z-1}, \\ H_\Delta(z) = \dfrac{z-1}{z}. \end{cases} \quad (1)$$

The MPP tracker in Fig. 2 can operate at different frequencies. The possibility of changing the frequency for the MPP tracker allows for a more realistic simulation. It is necessary for all ZOH (Zero-Order Hold) and transfer function blocks of Fig. 2 to operate at a same frequency.

B. Phase Locked Loop (PLL)

PSIM simulator has its own PLL block for grid-tied inverter systems. However, to simulate a digital controller and then derive its corresponding difference equations, it is suggested to use the structure of Fig. 3, presented in [28]. Note that a constant parameter ψ is added to the block diagram here, which will be discussed later.

The block diagram of Fig. 3 contains multiple transfer functions including an orthogonal signal generator, a PI compensator, and an integrator. Each z-domain TF has been derived from its corresponding s-domain TF using the Tustin method, as mentioned in [34]. Initially, the s-domain TFs of

the integrator and PI compensator are presented in (2). Hence, the corresponding z-domain TFs can be expressed as (3), regarding the sampling frequency f_{sa}:

$$\begin{cases} H_{PI}(s) = k_{PI} + \dfrac{k_{PI}}{sT_{PI}}, \\ H_I(s) = \dfrac{1}{s}. \end{cases} \quad (2)$$

$$\begin{cases} H_{PI}(z) = \dfrac{C_1 z + C_2}{z - 1}, \\ H_I(z) = \dfrac{C_3 z + C_3}{z - 1}. \end{cases} \quad (3)$$

Where the coefficients can be expressed as:

$$\begin{cases} C_1 = \dfrac{k_{PI}T_{sa}}{2T_{PI}} + k_{PI}, \quad C_2 = \dfrac{k_{PI}T_{sa}}{2T_{PI}} - k_{PI}, \\ C_3 = \dfrac{T_{sa}}{2}, \qquad\qquad T_{sa} = \dfrac{1}{f_{sa}}. \end{cases} \quad (4)$$
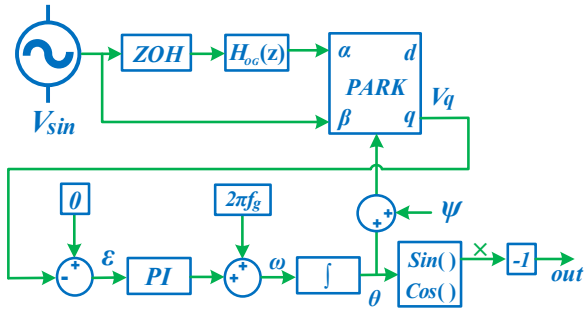
Fig. 3. The block diagram of the PLL.

Eventually, the difference equations of the PI compensator and the integrator are presented in (5) and (6), respectively. It is worth to mention that y[n] represents the output signal of the PI controller.

$$y[n] = C_1 \, \varepsilon[n] + C_2 \, \varepsilon[n - 1] + y[n - 1]. \quad (5)$$

$$\theta[n] = C_3 \, \omega[n] + C_3 \, \omega[n - 1] + \theta[n - 1]. \quad (6)$$

These difference equations can be easily implemented on a digital microcontroller device. A TI C2000 microcontroller is a proper choice due to its typically fast code execution capability.

At this point, it is appropriate to present the TF of the orthogonal signal generator. An orthogonal signal has the same amplitude as the primary signal, but a 90-degree phase shift. Therefore, two low-pass filters with the same cut-off frequency ω_c next to each other can be considered an orthogonal signal generator.

$$H_{OG}(s) = 2\left(\dfrac{\omega_c}{s + \omega_c}\right)^2. \quad (7)$$

Consequently, the z-domain TF of the orthogonal generator can be derived using Tustin method, as follows:

$$H_{OG}(z) = \dfrac{C_4 z^2 + 2C_4 z + C_4}{z^2 + 2C_5 z + C_5{}^2}. \quad (8)$$

Where the coefficients can be calculated using following equation set:

$$\begin{cases} C_4 = 2\left(\dfrac{\omega_c T_{sa}}{2 + \omega_c T_{sa}}\right)^2, \\ C_5 = \dfrac{\omega_c T_{sa} - 2}{\omega_c T_{sa} + 2}. \end{cases} \quad (9)$$

Now, the difference equation of the orthogonal signal generator, the last component of the PLL, is formulated in Equation (10) using expression (8). According to Fig. 3, the orthogonal signal α can be calculated as follows.

$$\alpha[n] = C_4 \, \alpha_1[n] - \alpha_2[n]. \quad (10)$$

$$\begin{cases} \alpha_1[n] = \beta[n] + 2 \, \beta[n - 1] + \beta[n - 2], \\ \alpha_2[n] = 2C_5 \, \alpha[n - 1] + C_5{}^2 \, \alpha[n - 2]. \end{cases} \quad (11)$$

Fig. 4 indicates the flowchart of an executable program on a microcontroller device regarding expressions (5), (6), (10) and (11), and Fig. 3.

It has to be mentioned that the required variables are specified by the red color in Fig. 4, which must be defined already in a variable initializing function. Additionally, the θ variable is subject to a condition that ensures it will not grow infinitely. Note that the sensors and their associated circuits may produce an unwanted phase difference between the grid voltage and its measured waveform. To compensate this phase delay, a constant parameter (specified by ψ) is added to the flowchart in Fig. 4. Therefore, the mentioned problem can be fixed by replacing ψ with the measured phase delay, in practice.
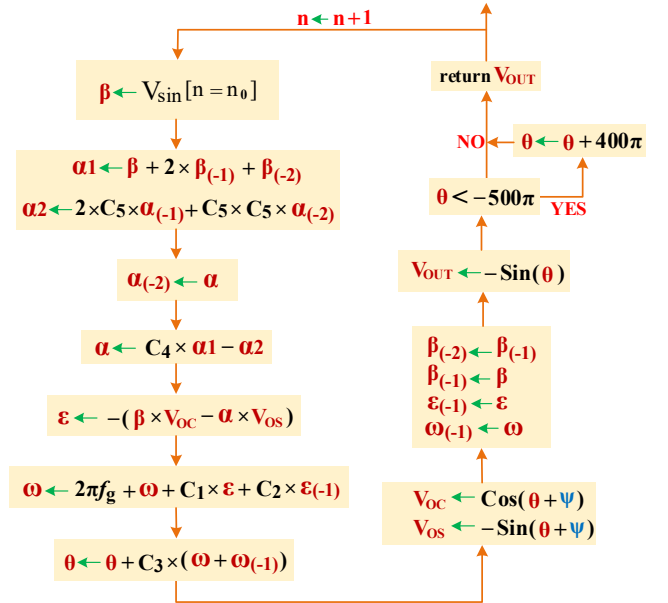
Fig. 4. The flowchart of the PLL algorithm implementable on a microcontroller device.

C. Inverter control loops

As Fig. 1 depicts, there are two control loops driving the inverter power switches. The inner control loop shapes the injected current to the grid, while the outer control loop regulates the DC bus voltage. The outer control loop includes a PI compensator, which was discussed earlier. Nonetheless, the inner current loop is going to be analyzed here due to the presence of a PR compensator. The expression (12) represents the s-domain TF of an ideal resonance compensator (RC).

$$H_{RC}(s) = \dfrac{k_r s}{s^2 + \omega_r{}^2}. \quad (12)$$

The coefficient k_r is $k\omega_r$, where k and ω_r represent the proportional coefficient and the resonance frequency of the PR controller, respectively. Although an infinite gain can provide zero steady state error, it is not a suitable choice due

to possible instability. Nonetheless, z-domain TF of an ideal resonance compensator is given in (13).

$$H_{RC}(z) = \frac{A_1 z^2 - A_2}{A_3 z^2 + A_4 z + A_5}. \tag{13}$$

$$\begin{cases} A_1 = A_2 = 2k_r T_{sa}, \\ A_4 = 2\omega_r^2 T_{sa}^2 - 8, \\ A_3 = A_5 = 4 + \omega_r^2 T_{sa}^2. \end{cases} \tag{14}$$

A non-ideal RC, on the other hand, has a larger bandwidth and lower gains comparing to the ideal version presented in (12). Moreover, its bandwidth can be controlled by its cut-off frequency, ω_c. Thus, the s-domain TF of the non-ideal resonance compensator can be expressed as follows:

$$H_{RC}(s) = \frac{k_r \omega_c s}{s^2 + 2\omega_c s + \omega_r^2}. \tag{15}$$

Using Tustin method for (15), the z-domain transfer function of a typical resonance compensator can be presented as:

$$H_{RC}(z) = \frac{A_1 z^2 - A_2}{z^2 + A_3 z + A_4}. \tag{16}$$

$$\begin{cases} A_1 = A_2 = \dfrac{2k_r \omega_c T_{sa}}{4 + 4\omega_c T_{sa} + \omega_r^2 T_{sa}^2}, \\ A_3 = \dfrac{2\omega_r^2 T_{sa}^2 - 8}{4 + 4\omega_c T_{sa} + \omega_r^2 T_{sa}^2}, \\ A_4 = \dfrac{4 - 4\omega_c T_{sa} + \omega_r^2 T_{sa}^2}{4 + 4\omega_c T_{sa} + \omega_r^2 T_{sa}^2}. \end{cases} \tag{17}$$

Eventually, a difference equation to implement a RC on a microcontroller device can be derived according to (17).

$$y[n] = A_1 x[n] - A_1 x[n-2] - A_3 y[n-1] - A_4 y[n-2]. \tag{18}$$

At this point, a current control loop can be implemented using this resonance compensator. This controller makes the inverter able to produce a sinusoidal current waveform with a given amplitude, and inject it to the utility grid. As mentioned earlier, the outer control loop regulates the DC bus voltage to a constant value of 400 V using a PI controller, which was discussed previously. This PI controller provides a reference current amplitude, proportional to the power drawn from the PV panels, for the inner control loop.

To explain how this current control loop works, the circuit diagram of the power section in Fig. 5 can be considered. This structure makes it possible to produce the desired current by generating a voltage with an amplitude approximately equal to that of the grid voltage. To prove this, it is assumed that the inverter has been designed properly and is capable of providing a standard low-harmonic sinusoidal voltage waveform. Assuming that the inverter current is linearly related to grid voltage by coefficient k_g for unity power factor, Fig. 5 suggests that:

$$\begin{cases} I_g(s) = \dfrac{V_{inv}(s) - V_g(s)}{s(L_{g1} + L_{g2})}, \\ I_g(s) = k_g V_g(s). \end{cases} \tag{19}$$

According to equation set (19), the amplitude of the inverter voltage for producing an in-phase current to the grid voltage can be calculated as (20).

$$\hat{V}_{inv} = \left(\sqrt{1 + (L_{g1} + L_{g2})^2 k_g^2} \right) \hat{V}_g \approx \hat{V}_g. \tag{20}$$
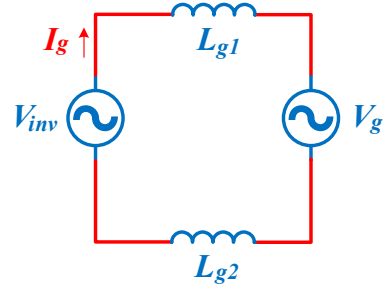
Fig. 5. The circuit diagram of the power section of a grid-connected inverter current control mechanism.

D. PWM Generator

Several switching patterns for HERIC inverters have been proposed in the literature. For the purposes of this paper, the switching pattern of Fig. 6 is an appropriate choice. This switching pattern allows inductor currents to flow in both directions, resulting in a low harmonic characteristic for the inverter voltage. Moreover, to avoid short circuit condition, a dead time ΔT is considered as indicated in Fig. 6. To realize a PWM generator in PSIM, the controller output m must be connected to the positive input of a comparator whose other input is a 20 kHz triangular carrier signal.
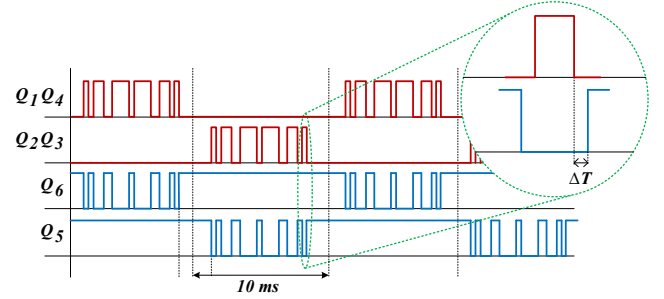
Fig. 6. Switching pattern of HERIC inverter.

III. DYNAMIC ANALYSIS OF A GRID-TIED INVERTER SYSTEM

This section presents the transient response of a grid-tied inverter system fed by a constant DC input source at the DC bus. It is assumed that the PLL block is enabled before the current controller, which is easy to implement. Thus, the PLL block has reached its steady state, and its dynamics no longer affect the transient response of the overall system. Moreover, the PI compensator of the DC bus is removed due to the replacement of the set of the PV panel and the boost converter with a constant DC voltage source. Therefore, the amplitude of the grid current must be given to the controller in this experiment. As it is mentioned earlier, the current controller contains a non-ideal PR compensator. Fig. 7 indicates the block diagram of the proposed system.
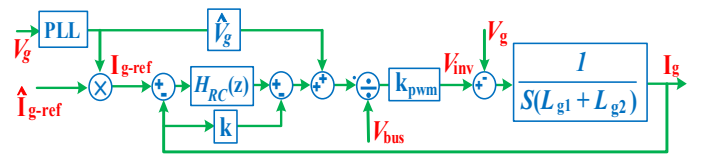
Fig. 7. Block diagram of the grid-tied inverter system being fed by a constant DC input source.

The block diagram of Fig. 7 results in a transfer function that explains the behavior of the system. Therefore, using this block diagram and the expression (15), it can be written that:

$$I_g = \frac{A_1 s^2 + A_2 s + A_3}{A_4 s^3 + A_5 s^2 + A_6 s + A_7} I_{g-ref}. \tag{21}$$

Where its coefficients are identified in (22). It is assumed that the grid voltage V_g is linearly related to the reference current I_{g-ref} by the coefficient k_g, as Fig. 7 suggests. In addition, the PWM coefficients k_{pwm} is defined as $V_{dc}/\hat{V}_{tri}$, where $\hat{V}_{tri}$ is the amplitude of the carrier signal.

$$\begin{cases} A_1 = k_{pwm} - V_{dc}, \\ A_2 = 2\omega_c k_{pwm} - 2\omega_c V_{dc} + k_r k_g k_{pwm}\omega_c, \\ A_3 = \omega_r^2(k_{pwm} - V_{dc}), \quad A_4 = k_g(L_{g1} + L_{g2})V_{dc}, \\ A_5 = (kk_{pwm} + 2\omega_c(L_{g1} + L_{g2})V_{dc})k_g, \\ A_6 = (2kk_{pwm}\omega_c + (L_{g1} + L_{g2})\omega_r^2 V_{dc} + k_r k_{pwm}\omega_c)k_g, \\ A_7 = kk_g k_{pwm}\omega_r^2. \end{cases} \tag{22}$$

The function of the inverter system can be analyzed using the transfer function (21). Supposing that this transfer function is fed by a proper input in PSIM simulator, its response can be plotted for different values of its key parameters, which are involved in shaping the transient and steady state characteristics. Note that all simulations of this paper have been conducted using the values of table I.

TABLE I. SPECIFICATIONS OF THE PV SYSTEM

	Parameter description	Symbol	Value
Boost converter	Boost inductor	L_b	$1\ mH$
	DC bus capacitor	C_{bus}	$2.5\ mF$
	DC Bus reference voltage	$V_{bus-ref}$	$10\ V$
	Feedback ratio	k_{bus}	0.025
	MPPT frequency	f_{MPPT}	$5\ kHz$
	Switching frequency	f_s	$20\ kHz$
Inverter	Output inductors	L_1, L_2	$500\ \mu H$
	Output capacitor	C_o	$10 \mu F$
	Controllers sampling frequency	f_{sa}	$20\ kHz$
	Switching frequency	f_s	$20\ kHz$
Grid	Grid inductors	L_{g1}, L_{g2}	$1.8\ mH$
	Grid voltage amplitude	$\hat{V}_g$	$320\ V$
	Grid frequency	f_g	$50\ Hz$
PLL	Proportional gain	k_{PI}	100
	Time constant	T_{PI}	0.01
	Cut-off frequency	ω_c	$100\pi\ Hz$
PR controller	Proportional gain	k	4
	Resonance frequency	ω_r	$100\pi\ Hz$
	Cut-off frequency	ω_c	$0.05 \times \omega_r$
PI controller	Proportional gain	k_{PI}	0.1
	Time constant	T_{PI}	0.01

Fig. 8 demonstrates the impact of the proportional gain of PR compensator, k, on the transient and steady states behavior of the system, based on a mathematical analysis. Although this approach clearly approves the proper operation

of the PR compensator, it is conducted under ideal conditions. Moreover, it does not contain the PV panel and MPPT. Therefore, to complete this mathematical approach, the inverter system in Fig. 1 can be simulated in PSIM.
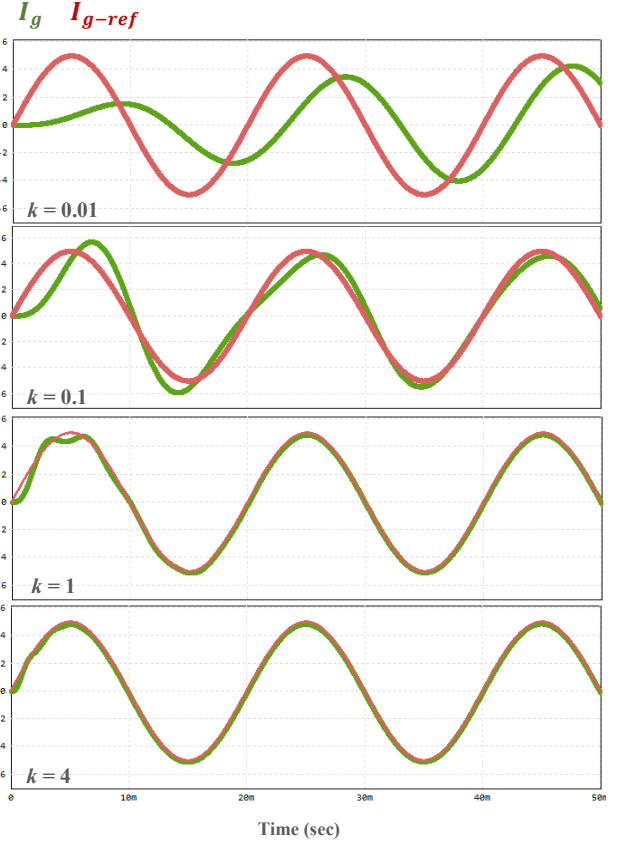

Fig. 8. Reference and actual waveforms of injected current to the grid for different proportional gains of PR compensator.

IV. SIMULATION RESULTS

MPP trackers obtain the instantaneous maximum power of the PV panel in inverter systems. Since the DC bus voltage and the effective value of the grid voltage are kept constant, the impact of irradiation variations on the solar panel is reflected in the effective value of the injected current to the grid. A mathematical study of the power flow of the overall inverter system, presented in [29], confirms this.

To study the impact of irradiation on the DC bus voltage and grid current, smooth and sudden changes in irradiation are applied to the solar panel. A well-designed control system has to maintain the DC bus voltage, and properly change the grid current effective value regarding the new value of irradiation. Fig. 9 indicates both of these desired operations are achieved after some transients.

Fig. 9 shows that the actual power drawn from the panel, as indicated by the green signal, tracks the maximum power of the panel, as indicated by the red reference signal, according to the MPPT algorithm. This is achieved for both smooth and sudden changes in irradiation.

Eventually, Fig. 10 shows the gate signals of some of the power switches of the inverter, and the voltage waveform it produces right before the grid inductors. To realize the exact function of the current controller, an interesting experiment is suggested. In the inverter system without a PV panel and

boost converter, as shown in Fig. 5, the grid inductors are replaced with a 15 Ω resistor. In addition, the grid reference current is set to 4 A. Thus, in spite of the configuration in Fig. 5, the required inverter voltage to produce the desired current waveform on this 15 Ω resistor must be high enough to be observable. This experiment provides a simple explanation of the current controller function due to the significant difference between the grid and inverter voltage waveforms, as Fig. 11 depicts.
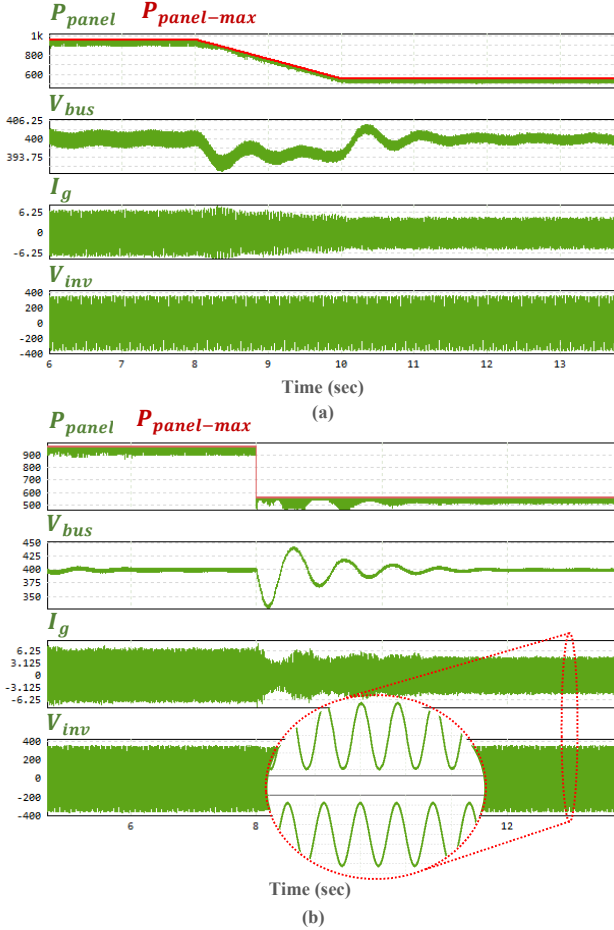

Fig. 9. Panel power, bus voltage, and grid current waveforms of the PV-based inverter system, while irradiation changes are applied a) a smooth change b) a sudden or step change.
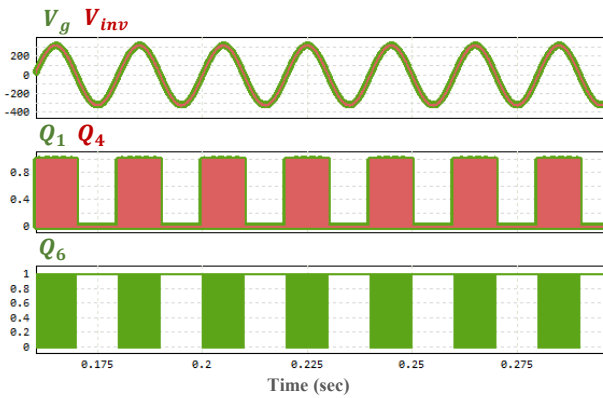
Fig. 10. Waveforms of the grid and inverter voltages and gate pulses of a main and a commutation power switch.
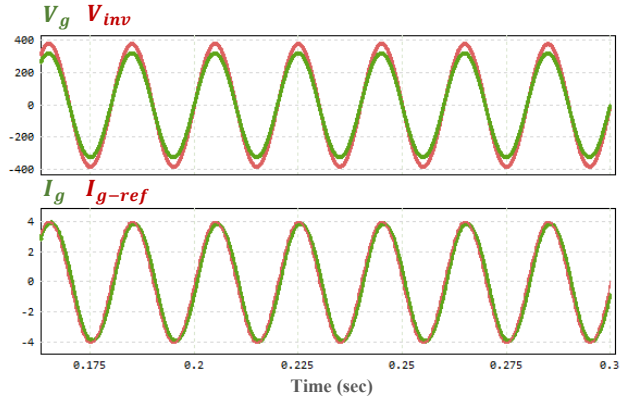
Fig. 11. Grid and inverter voltage and current waveforms while a 15 Ω resistor is placed between them instead of inductors L_{g1} and L_{g2}, and the set of PV panel and boost converter is replaced by a input DC voltage source.

V. CONCLUSION

This article analyzed and simulated a digital control strategy for photovoltaic-based inverter systems in the z-domain. Furthermore, its transient responses are investigated under some different conditions of irradiation. To provide a precise explanation of the system, a mathematical approach to derive the dynamic response of a grid-tied inverter configuration was also presented. Eventually, simulation results were provided to verify the claims and analyses.

REFERENCES

[1] Alghaythi, M.L., O'Connell, R.M., Islam, N.E., Khan, M.M.S. and Guerrero, J.M., 2020. A high step-up interleaved DC-DC converter with voltage multiplier and coupled inductors for renewable energy systems. *IEEE Access*, *8*, pp.123165-123174.

[2] Altimania, M., Alzahrani, A., Ferdowsi, M. and Shamsi, P., 2019, February. Operation and analysis of non-isolated high-voltage-gain DC-DC boost converter with voltage multiplier in the DCM. In *2019 IEEE Power and Energy Conference at Illinois (PECI)* (pp. 1-6). IEEE.

[3] Athikkal, S., Sehgal, K., Mohan, U. and Singh, A., 2020, September. A voltage multiplier based non isolated high gain DC-DC converter for DC bus application. In *2020 International Conference on Futuristic Technologies in Control Systems & Renewable Energy (ICFCR)* (pp. 1-6). IEEE.

[4] Azizkandi, M.E., Sedaghati, F., Shayeghi, H. and Blaabjerg, F., 2019. A high voltage gain DC–DC converter based on three winding coupled inductor and voltage multiplier cell. *IEEE Transactions on Power Electronics*, *35*(5), pp.4558-4567.

[5] Mohseni, P., Hosseini, S.H. and Maalandish, M., 2019. A new soft switching DC–DC converter with high voltage gain capability. *IEEE Transactions on Industrial Electronics*, *67*(9), pp.7386-7398.

[6] Schmitz, L., Martins, D.C. and Coelho, R.F., 2020. Comprehensive conception of high step-up DC–DC converters with coupled inductor and voltage multipliers techniques. *IEEE Transactions on Circuits and Systems I: Regular Papers*, *67*(6), pp.2140-2151.

[7] Wu, G., Ruan, X. and Ye, Z., 2017. High step-up DC–DC converter based on switched capacitor and coupled inductor. *IEEE transactions on industrial electronics*, *65*(7), pp.5572-5579.

[8] Forouzesh, M., Shen, Y., Yari, K., Siwakoti, Y.P. and Blaabjerg, F., 2017. High-efficiency high step-up DC–DC converter with dual coupled inductors for grid-connected photovoltaic systems. *IEEE Transactions on Power Electronics*, *33*(7), pp.5967-5982.

[9] Meraj, M., Bhaskar, M.S., Iqbal, A., Al-Emadi, N. and Rahman, S., 2020. Interleaved multilevel boost converter with minimal voltage multiplier components for high-voltage step-up applications. *IEEE Transactions on Power Electronics*, *35*(12), pp.12816-12833.

[10] Li, G., Jin, X., Chen, X. and Mu, X., 2020. A novel quadratic boost converter with low inductor currents. *cpss transactions on power electronics and applications*, *5*(1), pp.1-10.

[11] Veerachary, M., 2017, December. Design and analysis of a new quadratic boost converter. In *2017 National Power Electronics Conference (NPEC)* (pp. 307-313). IEEE.

[12] Zhang, X., Sun, L., Guan, Y., Han, S., Cai, H., Wang, Y. and Xu, D., 2020. Novel high step-up soft-switching DC–DC converter based on switched capacitor and coupled inductor. *IEEE Transactions on Power Electronics*, *35*(9), pp.9471-9481.

[13] Mohseni, P., Dezhbord, M., Islam, M.R., Xu, W. and Muttaqi, K.M., 2021. Interleaved ultra-high step-up DC-DC converters with extendable voltage gains and ZVS performance. *IEEE Access*, *9*, pp.129417-129430.

[14] Nouri, T., Kurdkandi, N.V. and Shaneh, M., 2020. A novel ZVS high-step-up converter with built-in transformer voltage multiplier cell. *IEEE Transactions on Power Electronics*, *35*(12), pp.12871-12886.

[15] Ajami, A., Ardi, H. and Farakhor, A., 2014. A novel high step-up DC/DC converter based on integrating coupled inductor and switched-capacitor techniques for renewable energy applications. *IEEE Transactions on Power Electronics*, *30*(8), pp.4255-4263.

[16] Hassan, W., Lu, D.D.C. and Xiao, W., 2019. Single-switch high step-up DC–DC converter with low and steady switch voltage stress. *IEEE Transactions on Industrial Electronics*, *66*(12), pp.9326-9338.

[17] Rahimi, R., Habibi, S., Ferdowsi, M. and Shamsi, P., 2021. An interleaved quadratic high step-up DC-DC converter with coupled inductor. *IEEE Open Journal of Power Electronics*, *2*, pp.647-658.

[18] Hu, S., Li, C., Li, W., He, X. and Cao, F., 2015, September. Enhanced HERIC based transformerless inverter with hybrid clamping cell for leakage current elimination. In *2015 IEEE energy conversion congress and exposition (ECCE)* (pp. 5337-5341). IEEE.

[19] Wang, H., Wu, Z., Tang, Z., Han, H., Yang, Y. and Blaabjerg, F., 2019, March. An improved modulation strategy for the active voltage clamping HERIC inverter. In *2019 IEEE Applied Power Electronics Conference and Exposition (APEC)* (pp. 1938-1942). IEEE.

[20] Tang, Z., Yang, Y., Su, M., Jiang, T., Blaabjerg, F., Dan, H. and Liang, X., 2019. Modulation for the AVC-HERIC inverter to compensate for deadtime and minimum pulsewidth limitation distortions. *IEEE Transactions on Power Electronics*, *35*(3), pp.2571-2584.

[21] Bighash, E.Z., Sadeghzadeh, S.M., Ebrahimzadeh, E. and Blaabjerg, F., 2017, October. LVRT capability of single-phase grid-connected HERIC inverter in PV systems by a look-up table based predictive control. In *IECON 2017-43rd Annual Conference of the IEEE Industrial Electronics Society* (pp. 2570-2575). IEEE.

[22] Freddy, T.K.S., Lee, J.H., Moon, H.C., Lee, K.B. and Abd Rahim, N., 2017. Modulation technique for single-phase transformerless photovoltaic inverters with reactive power capability. *IEEE transactions on industrial electronics*, *64*(9), pp.6989-6999.

[23] Zaid, S.A. and Kassem, A.M., 2017. Review, analysis and improving the utilization factor of a PV-grid connected system via HERIC transformerless approach. *Renewable and Sustainable Energy Reviews*, *73*, pp.1061-1069.

[24] Esram, T. and Chapman, P.L., 2007. Comparison of photovoltaic array maximum power point tracking techniques. *IEEE Transactions on energy conversion*, *22*(2), pp.439-449.

[25] Subudhi, B. and Pradhan, R., 2012. A comparative study on maximum power point tracking techniques for photovoltaic power systems. *IEEE transactions on Sustainable Energy*, *4*(1), pp.89-98.

[26] De Brito, M.A., Sampaio, L.P., Luigi, G., e Melo, G.A. and Canesin, C.A., 2011, June. Comparative analysis of MPPT techniques for PV applications. In *2011 International Conference on Clean Electrical Power (ICCEP)* (pp. 99-104). IEEE.

[27] Nicastri, A. and Nagliero, A., 2010, July. Comparison and evaluation of the PLL techniques for the design of the grid-connected inverter systems. In *2010 IEEE International Symposium on Industrial Electronics* (pp. 3865-3870). IEEE.

[28] Picardi, C., Sgro, D. and Gioffre, G., 2010, June. A simple and low-cost PLL structure for single-phase grid-connected inverters. In *SPEEDAM 2010* (pp. 358-362). IEEE.

[29] Zakzouk, N.E., Abdelsalam, A.K., Helal, A.A. and Williams, B.W., 2016. PV single-phase grid-connected converter: DC-link voltage sensorless prospective. *IEEE Journal of Emerging and Selected Topics in Power Electronics*, *5*(1), pp.526-546.

[30] Busarello, T.D.C., Pomilio, J.A. and Simoes, M.G., 2018, December. Design procedure for a digital proportional-resonant current controller in a grid connected inverter. In *2018 IEEE 4th Southern Power Electronics Conference (SPEC)* (pp. 1-8). IEEE.

[31] Sato, Y., Ishizuka, T., Nezu, K. and Kataoka, T., 1998. A new control strategy for voltage-type PWM rectifiers to realize zero steady-state control error in input current. *IEEE Transactions on Industry Applications*, *34*(3), pp.480-486.

[32] Husev, O., Roncero-Clemente, C., Makovenko, E., Pimentel, S.P., Vinnikov, D. and Martins, J., 2019. Optimization and implementation of the proportional-resonant controller for grid-connected inverter with significant computation delay. *IEEE Transactions on Industrial Electronics*, *67*(2), pp.1201-1211.

[33] Cossoli, P., Cáceres, M., Vera, L., Firman, A. and Busso, A., 2018, September. Proportional-resonant controller and LCL filter design for single-phase grid-connected PV micro-inverters. In *2018 IEEE PES Transmission & Distribution Conference and Exhibition-Latin America (T&D-LA)* (pp. 1-5). IEEE.

[34] Rodriguez, F.J., Bueno, E., Aredes, M., Rolim, L.G.B., Neves, F.A. and Cavalcanti, M.C., 2008, November. Discrete-time implementation of second order generalized integrators for grid converters. In *2008 34th Annual Conference of IEEE Industrial Electronics* (pp. 176-181). IEEE.